LabonaChip

Microfluidics-enabled rational design of immunomagnetic nanomaterial and its shape effect in liquid biopsy

SCHOLARONE™
Manuscripts

Lab on a Chip

Microfluidics-enabled rational design of immunomagnetic nanomaterial and its shape effect in liquid biopsy

Nanjing Hao[1], Yuan Nie[1], Ting Shen[2] and John X.J. Zhang[1]*

Microfluidics brings unique opportunities for nanomaterials synthesis toward efficient liquid biopsy. Herein, we developed microreactor-enabled flow synthesis of immunomagnetic nanomaterials with controllable shapes (sphere, cube, rod, and belt) by simply tuning the flow rates. The particle shape-dependent screening efficiency of circulating tumor cells was first investigated and compared with commercial ferrofluid, providing new insights for the rational design of particulate system toward the screening and analysis of circulating tumor biomarkers.

Circulating tumor cells (CTCs) as emerging noninvasive tumor biomarker offer great potential alternative to conventional invasive tissue biopsies for early cancer detection. Recent studies revealed that CTCs-based liquid biopsy could act as a reliable means to monitor real-time cancer progress and predict metastasis development.[1–3] The screening process of CTCs usually involves specific capture and enrichment from background normal hematocytes, where the most challenging aspect is the natural extreme rareness of CTCs.[4] Among a variety of available screening approaches based on mechanisms such as dielectrophoresis, filtration, inertial force, acoustophoresis, antibody-mediated immunoassay, and immunomagnetic assay,[3,5–11] the immunomagnetic screening approach that works by selectively labeling the CTCs with antibody-conjugated magnetic nanoparticles and the subsequent capture by applying an external magnetic field has attracted great attention due to its relative high specificity, good sensitivity, and low detection limit.[12] Actually, immunomagnetic approach still represents one of the most successful techniques, especially the CellSearch[TM] system that employs EpCAM-conjugated magnetic nanoparticles for CTCs capture became the first validated CTCs assay approved by the US Food and Drug Administration (FDA).[3,13,14] In addition, the advent of microchip-based immunomagnetic assay that combines the benefits of microfluidic and immunomagnetic techniques makes the screening process achieve higher throughput and more efficient performance.[15–18] However, although great achievement has been made, it is noted that the structure effect of immunomagnetic nanomaterials on the screening efficiency of CTCs is still not systematically investigated.

Recent studies from both experimental and theoretical aspects have already revealed that the shapes of nanomaterials could significantly affect their biological performance, especially the cellular binding kinetics.[19–22] We thus assumed that particle shape of immunomagnetic nanomaterials plays a significant role in the screening efficiency of CTCs, in other words, the screening performance can be improved through the rational design of immunomagnetic nanomaterials. Recently, microfluidic technique is also showing great promise in chemical synthesis.[23–25] Compared to conventional batch reactors, microfluidics-based microreactors exhibit many unique and appealing features, such as precise and automatic flow control for minimizing the local variations and easy scaleout, intensive and sufficient mixing of reactants for achieving high yields, rapid reaction kinetics for fast identification and optimization of synthesis parameters, and feasible integration capability for inline measurement.[26–29] Given these, microfluidic reactors may provide new and unique opportunities for the controllable synthesis of immunomagnetic nanomaterials toward the screening of CTCs.

In this study, we first developed a facile and straightforward flow synthesis strategy to create immunomagnetic nanomaterials with four distinct shapes (sphere, cube, rod, and belt) and examined the shape effect of immunomagnetic nanomaterials on the screening performance of CTCs (Figure 1A). Magnetic nanoparticles (MNPs) of different shapes were firstly synthesized via a miniaturized spiral-shaped microfluidic device by simply tuning the flow rates (Figure 1A, Step I). Silica shell was then homogeneously coated on MNPs for stabilizing their structures and conjugating targeting antibodies (Figure 1A, Step II). The resultant immunomagnetic nanomaterials

[1]Thayer School of Engineering, Dartmouth College, 14 Engineering Drive, Hanover, New Hampshire 03755, United States. E-mail: john.zhang@dartmouth.edu
[2]NanoLite Systems, 1521 Concord Pike, Wilmington, DE 19803, United States.
Electronic Supplementary Information (ESI) available: [details of any supplementary information available should be included here]. See DOI: 10.1039/x0xx00000x

Please do not adjust margins
Lab on a Chip
Page 2 of 7

were subsequently used to examine the effect of particle shape on the screening efficiency of tumor cells-spiked whole blood samples using the CellRich[TM] microchip developed earlier from our lab, which has been licensed to NanoLite Systems, Inc. (Figure 1A, Step III).[15–18] The captured tumor cells were finally identified and enumerated (Figure 1A, Step IV) and the results were compared to the standard CellSearch[TM] system.
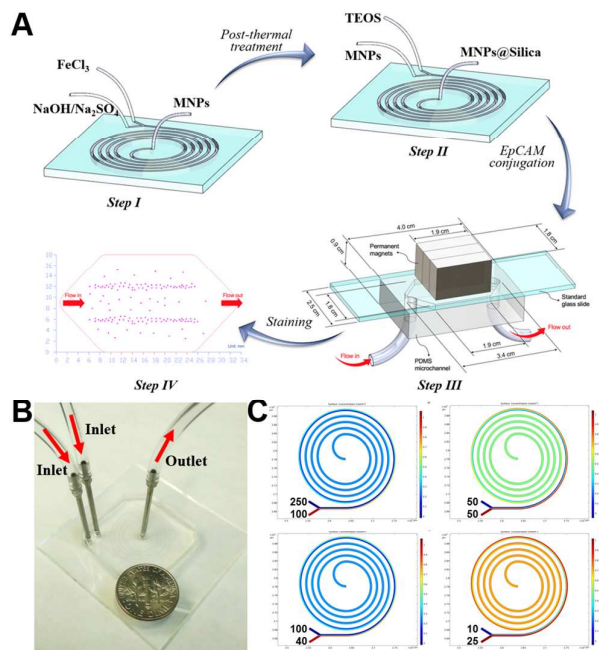
Figure 1. (A) Schematic workflow showing the step-by-step process of microfluidics-mediated controllable synthesis of immunomagnetic nanomaterials toward CTCs screening. (B) The photograph showing the microfluidic device used in this study, with a U.S. one dime coin for scale. (C) Simulation results of mixing at different flow rates (μL/min) in microfluidic spiral channel, where two flows having different concentrations could achieve complete mixing within about one run (see details in SI).

Microfluidics-enabled flow synthesis of MNPs was carried out on the basis of the spiral-shaped five-run microreactor with two inlets and one outlet (Figure 1B). The spiral-shaped microchannel pattern was chosen mainly because of its well-demonstrated rapid and efficient mixing compared to other geometric patterns such as expansion and contraction pattern, circular serpentine pattern, and rectangular serpentine pattern.[26–29] The smallest microchannel diameter in such microreactor is 5.25 mm and then it increases from 11.0 mm to 22.2 mm with an increment of 1.4 mm for each half run. The height and width of the microchannel are 50 and 500 μm, respectively. The two inlet flows, one containing ferric chloride (FeCl$_3$, 0.02 M in water) and the other sodium hydroxide and sodium sulfate (NaOH/Na$_2$SO$_4$, both at 0.06 M in water), were pumped (Harvard Apparatus, Pump 33 DDS) into the spiral-shaped microreactor at room temperature. The products were collected from the outlet for further post-thermal treatment

and analysis (see details in SI), and the shapes of MNPs were expected to be regulated by the flow rates of two inlets.
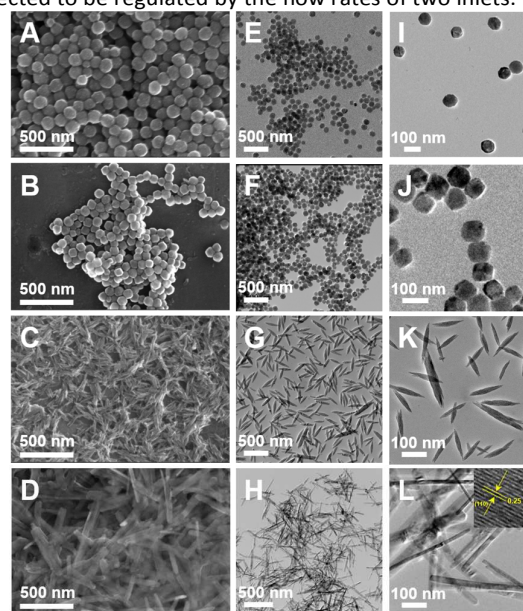

Figure 2. Scanning electron microscopy (SEM, A–D) and transmission electron microscopy (TEM, E–L) images of as-synthesized sMNPs (A&E&I), cMNPs (B&F&J), rMNPs (C&G&K), and bMNPs (D&H&L). Representative lattice pattern was shown in the inlet of figure L.

Compared to the previous day-scale synthesis of iron oxide nanoparticles,[30–32] microreactor brings many superior advantages to produce iron oxide nanoparticles even in a seconds-scale (see details in SI). Besides of the faster reaction kinetics, the relatively low Reynolds number of microreactors also permits the intensive and efficient mixing of reaction fluids (Figure 1C).[27,33] As shown in Figure 2, such microreactor can be successfully used to yield well-defined sphere-, cube-, rod-, and belt-shaped MNPs (denoted as sMNPs, cMNPs, rMNPs, and bMNPs, respectively). sMNPs having an average diameter of 91 nm were obtained when the flow rates of FeCl$_3$ fluid and NaOH/Na$_2$SO$_4$ fluid were set as 250 and 100 μL/min, respectively (Figure 1A&E&I). cMNPs with an average side length of 83 nm were fabricated when both flow rates were set as 50 μL/min (Figure 1B&F&J). rMNPs that have an average width of 42 nm and an average length of 207 nm were synthesized when the flow rates of FeCl$_3$ fluid and NaOH/Na$_2$SO$_4$ fluid were set as 100 and 40 μL/min, respectively (Figure 1C&G&K). bMNPs showing an average height, width, and length of 20, 46, and 354 nm respectively were yielded when the flow rates of FeCl$_3$ fluid and NaOH/Na$_2$SO$_4$ fluid were maintained at 10 and 25 μL/min, respectively (Figure 1D&H&L). Such successful shape transformation achieved by simply tuning the flow rates could be mainly attributed to the change of ferric ions concentration, pH (NaOH concentration), and sulfate species concentration at the interface of two reactant flows, which further determined the nucleation and growth of hematite nanoparticles.[30–32] Specifically, higher flow rate of FeCl$_3$ fluid generates higher

COMMUNICATION

concentration of precursor with faster reaction kinetics and thus generally forms larger sized isotropic particles, whereas, lower flow rate of NaOH/Na$_2$SO$_4$ fluid brings relatively weaker basic condition with slower reaction kinetics and thus produces smaller sized anisotropic particles.[30] These four kinds of monodispersed iron oxide nanomaterials exhibited distinctly different structures, which provide the basic platform for revealing the shape effect of MNPs on the screening performance of CTCs.

To further stabilize the magnetic structures, improve their biocompatibility, and ease the surface conjugation,[34,35] MNPs surface was coated with a layer of silica to make magnetic core-silica shell nanocomposite (MNPs@Silica). The superior intensive and efficient mixing performance endows microreactor an ideal system to hydrolyze silica precursor tetraethyl orthosilicate (TEOS) and to subsequently condense on iron oxide nanoparticle surface to form the silica shell. As shown in Figure 3A-H, when using the same spiral-shaped five-run microreactor but with one inlet flow containing MNPs (1 mg/mL in diluted ammonia) and the other TEOS (45 mM in ethanol) at the same flow rate of 50 μL/min, the well-defined sphere-, cube-, rod-, and belt-shaped core-shell structures (denoted as sMNPs@Silica, cMNPs@Silica, rMNPs@Silica, and bMNPs@Silica, respectively) can be successfully synthesized. After removing the magnetic core by the hydrochloride (see details in SI), the typical hollow silica nanostructures further confirmed the establishment of all these four kinds of core-shell nanocomposites from microreactor (Figure 3I). In addition, the silica shell thickness can be also well-tuned by changing the flow rates of TEOS fluid. The lower the flow rate of TEOS, the thicker the shell of MNPs@Silica (Figure 3J). Since the thickness of silica layer significantly affects the resultant stability and magnetism,[34,35] MNPs@Silica with a shell thickness of 5-10 nm (when both flow rates were maintained at 50 μL/min) were chosen for the following analysis. The magnetic hysteresis of MNPs@Silica with different shapes was examined using the vibrational sample magnetometer (VSM), the saturation magnetization values of sMNPs@Silica, cMNPs@Silica, rMNPs@Silica, and bMNPs@Silica are at around 5-10 emu/g Fe (Figure S1). Given their similar physicochemical property, these MNPs@Silica will be good candidates to examine the roles of particle shape on the CTCs screening.
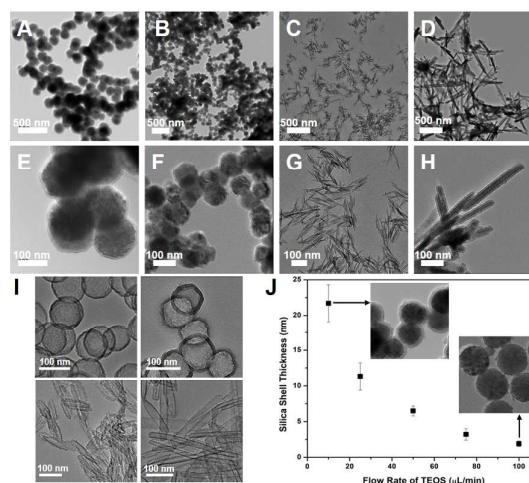
Figure 3. (A-H) TEM images of as-synthesized core-shell sMNPs@Silica (A&E), cMNPs@Silica (B&F), rMNPs@Silica (C&G), and bMNPs@Silica (D&H) at different magnifications. (I) TEM images of the corresponding hollow silica shell nanostructure after removing MNPs core. (J) Examples of silica shell thickness control on sMNPs by varying the flow rate of TEOS, the insets are two TEM images showing the product at certain flow rate of TEOS.

Given that most assays established so far for the enumeration of CTCs, including the gold standard CellSearch[TM, 14] rely on the expression of the cell surface biomarker epithelial cell adhesion molecule (EpCAM), we functionalized the MNPs@Silica particle surface with FITC-conjugated Anti-EpCAM (MNPs@Silica-EpCAM, see details in SI, Figure S2). The FITC conjugates from EpCAM antibody help not only in demonstrating the successful functionalization, but more importantly, in tracking the location of these MNPs@Silica-EpCAM after treated with cells. Two kinds of human breast cancer cell lines, MCF-7 and MDA-MB-231, were investigated in this study. MCF-7 cells express high levels of EpCAM (EpCAM[pos]) while MDA-MB-231 cells express no/low levels of EpCAM (EpCAM[low/neg]).[36]

Please do not adjust margins
Lab on a Chip
Page 4 of 7
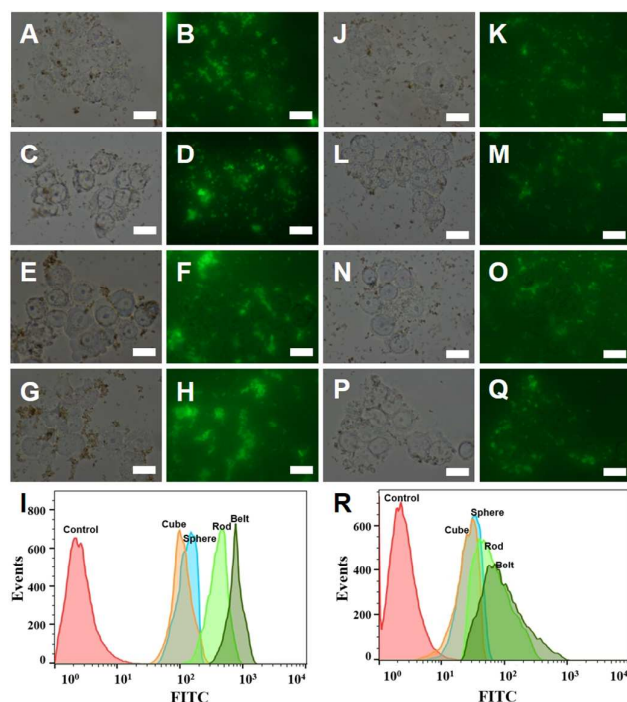
Figure 4. Cellular binding efficiency of sMNPs@Silica-EpCAM, cMNPs@Silica-EpCAM, rMNPs@Silica-EpCAM, and bMNPs@Silica-EpCAM. (A-I) Bright field and fluorescent images of magnetic sphere- (A&B), cube- (C&D), rod- (E&F), and belt- (G&H) treated MCF-7 cells, and the corresponding flow cytometry analysis results (I). (J-R) Bright field and fluorescent images of magnetic sphere- (J&K), cube- (L&M), rod- (N&O), and belt- (P&Q) treated MDA-MB-231 cells, and the corresponding flow cytometry analysis results (R). All scale bars represent a length of 20 μm.

The cytotoxicity of MNPs@Silica-EpCAM with different shapes was firstly examined on both cell lines, there was no obvious cellular toxicity observed at a broad particle concentration range of 0.1-1000 μg/mL (Figure S3, see experimental details in SI), indicating good cytocompatibility of MCF-7 and MDA-MB-231 with MNPs@Silica-EpCAM. The cellular binding kinetic of MNPs@Silica-EpCAM was then analyzed by flow cytometry to determine the optimal time for treating cells with nanoparticles. Flow cytometry could measure the fluorescence of individual cells and count the cell numbers that are above the cellular auto-fluorescence.[37] The results showed that both MCF-7 and MDA-MB-231 cells exhibit relatively fast binding kinetic rates toward such kind of immunomagnetic nanoparticles (Figure S4). Although the cellular binding rate was almost continuously increasing over 360 min, the rate of binding reached nearly 80-90% in one hour. We thus carried out cellular tests with one-hour particle treatment to study the shape effect of MNPs@Silica-EpCAM on cellular binding efficiency using fluorescence microcopy and flow cytometry. Results from fluorescence microcopy showed that both MCF-7 (Figure 4A-H) and MDA-MB-231 (Figure 4J-Q) cells could efficiently bind with differently shaped immunomagnetic nanoparticles. It is noted that, compared with cells treated by sphere- and cube-shaped particles, cells

treated by rod- and belt-shaped particles exhibit obviously stronger fluorescent intensity, indicating that the cellular binding amounts of rod- and belt-shaped particles are higher than that of sphere- and cube-shaped particles. In addition, MCF-7 cells showed stronger fluorescent intensity than MDA-MB-231 cells for all these four kinds of immunomagnetic nanoparticles, which was further confirmed by the quantitative results from flow cytometry (Figure 4I&R). The mean fluorescent intensity (MFI) values of sphere- and cube-treated MCF-7 cells were similar, but the MFI values of rod- and belt-treated MCF-7 cells were nearly four times and seven times of that of sphere-treated ones, respectively (Figure 4I). Similar MFI values were also observed for sphere- and cube-treated MDA-MB-231 cells, and the MFI values of rod- and belt- treated MDA-MB-231 cells were nearly two times and three times of that of sphere-treated ones, respectively (Figure 4R).These results demonstrated that the cell-nanoparticle interaction depends not only on cell types but also on the particle shapes where particles having longer aspect ratios produce better cellular binding performance.[19,20,38]
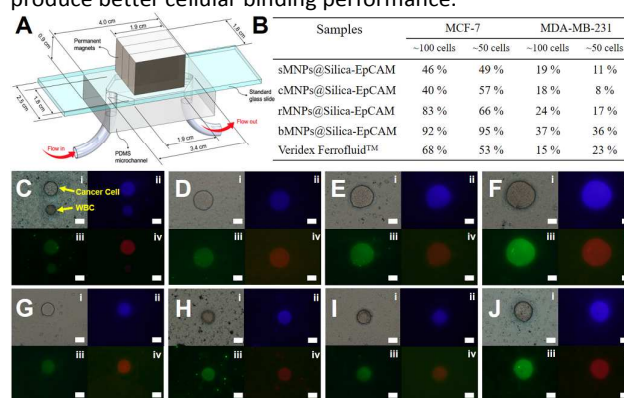
Figure 5. Microfluidics-based tumor cells screening. (A) Schematic image of the CellRich[TM] microchip (NanoLite Systems) for CTCs screening. (B) A comparison table showing screening efficiency of tumor cells spiked in whole blood samples. (C-F) Representative images of sphere- (C), cube- (D), rod- (E), and belt- (F) captured MCF-7 cells. (G-J) Representative images of sphere- (G), cube- (H), rod- (I), and belt- (J) captured MDA-MB-231 cells. Blue (marked as ii), green (marked as iii), and red color (marked as iv) came from Hoechst 33342, FITC-labeled MNPs@Silica-EpCAM, and Anti-Pan Cytokeratin eFluor® 615, respectively. All scale bars denote a length of 20 μm.

Based on the above observations, we employed MNPs@Silica-EpCAM and tumor cells-spiked whole blood samples to examine the effect of particle shape on the screening efficiency of CTCs through the CellRich[TM] microchip (Figure S5).[15–18,39] Figure 5A illustrates the integrated immunomagnetic CTCs screening system. A polydimethylsiloxane (PDMS) chip is bonded to a standard glass slide forming a hexagonal microchamber with a dimension of 34 × 18 × 0.5 mm. Three permanent magnets are placed outside the microfluidic device with alternating polarities, and the blood sample is introduced into the

Page 5 of 7
Please do not adjust margins
Lab on a Chip

COMMUNICATION

microchannel by a syringe pump. When the blood sample is flowed through the microchannel, immunomagnetic nanoparticles-labeled CTCs could be magnetically captured on the channel substrate, while normal hematocytes such as red blood cells (RBCs) and white blood cells (WBCs) could flow out of the microchannel. After the screening process, the captured CTCs fixed on glass slide surface could be immunofluorescently staining for identification, enumeration, and further studies.

To examine the screening efficiency of MNPs@Silica-EpCAM through our developed integrated microchip, MCF-7 and MDA-MB-231 cells of different numbers were separately spiked into normal human whole blood. Capture rate is defined as the ratio of cancer cell numbers captured in the screened samples to the average cancer cell numbers counted on three control slides that are prepared from the same cell suspension at the same time as the blood sample is spiked.[15–18,39] Specifically, when the screening blood sample is spiked with cancer cells, an equal aliquot volume of the same cell suspension is spread on glass slide as control samples for calculating the capture rates. The captured cells can be easily recognized under microscope, especially from the typical green fluorescent signal after cells treated with FITC-conjugated MNPs@Silica-EpCAM for 1 h. To further identify the cancer cells, the experimental slides were immunofluorescently stained with Hoechst 33342 (blue-fluorescent DNA probe) and Anti-Pan Cytokeratin eFluor® 615 (red-fluorescent cytokeratin probe). Cancer cells exhibit recognizable blue, green, and red color, while the main interfering WBCs only display blue and green color (Figure 5C). Thus we can be able to effectively tell WBCs from CTCs. As shown in Figure 5B-J, all these four kinds of immunomagnetic nanoparticles can be successfully employed to capture MCF-7 cells and MDA-MB-231 cells from whole blood samples at a flow rate of 2.5 mL/h. The particle shape-dependent screening efficiency of CTCs was confirmed. Among MNPs@Silica-EpCAM of different shapes, belt-shaped particles exhibited the highest capture rates for both cancer cell types and samples spiked with different number of cells, rod-shaped particles the second, and sphere- and cube-shaped particles the relatively lowest capture efficiency. The capture efficiency of MCF-7 cells was obviously higher than that of MDA-MB-231 cells. These observations are roughly in agreement with the above cellular binding efficiency results (Figure 4). Veridex Ferrofluid from CellSearch™ was also used to perform comparable screening tests. It was found that Veridex Ferrofluid generally possessed better capture performance of CTCs than sphere- and cube-shaped immunomagnetic nanoparticles, which may be mainly attributed to its smaller particle size (less than 50 nm, Figure S6) and thus higher binding efficiency toward cancer cells.[40,41] However, its capture efficiency of CTCs was generally lower than that of long aspect ratio rod- and belt-shaped MNPs@Silica-EpCAM. In addition, no false-positive cells were observed in experiments of normal blood samples without spiked cancer cells (data not shown). These results further demonstrated that particle shape of the immunomagnetic nanomaterials significantly affects their screening performance of CTCs, shedding new light on the design of particulate systems toward enhanced capability for capturing circulating tumor biomarkers.

Conclusions

In summary, we first developed a microfluidics-enabled strategy for controllable synthesis of immunomagnetic nanomaterials with different shapes and investigated the effect of particle shape on the screening efficiency of CTCs through our developed microchip. Magnetic nanoparticles having four distinct shapes including sphere, cube, rod, and belt can be facilely tuned through changing the flow rates of $FeCl_3$ and $NaOH/Na_2SO_4$ fluids in spiral-shaped microreactor by relying on its rapid and efficient mixing performance. Such microreactor was further successfully employed to coat silica layer on magnetic nanoparticle surface to form more stable and biocompatible MNPs@Silica core-shell structure with tunable shell thickness by changing the flow rate of TEOS fluid. Cellular binding efficiency of MNPs@Silica-EpCAM by MCF-7 and MDA-MB-231 cells depended on both cell types and particle shapes, which further determined the screening performance of immunomagnetic nanoparticles. It was found that belt-shaped nanoparticles having the largest aspect ratio exhibited the highest capture rates in tumor cells-spiked whole blood samples, rod-shaped nanoparticles the second, and sphere- and cube-shaped nanoparticles the relatively lowest capture efficiency. These findings not only provide new alternative routes for controllable synthesis of functional micro-/nanostructures via microreactors, but also bring new perspectives for the rational design of more effective immunomagnetic materials toward liquid biopsy.

Conflicts of interest

There are no conflicts of interests to declare.

Acknowledgements

References

1 S. K. Arya, B. Lim, A. R. A. Rahman, S. Data and S. Fig, *Lab Chip*, 2013, **13**, 1995–2027.

2 J. H. Myung and S. Hong, *Lab Chip*, 2015, **15**, 4500–4511.

3 N. Hao and J. X. J. Zhang, *Sep. Purif. Rev.*, 2018, **47**, 19–48.

4 C. Alix-Panabières and K. Pantel, *Nat. Rev. Cancer*, 2014, **14**, 623–631.

5 L. Hajba and A. Guttman, *Trends Anal. Chem.*, 2014, **59**, 9–16.

6 C. M. Earhart, C. E. Hughes, R. S. Gaster, C. C. Ooi, R. J. Wilson, L. Y. Zhou, E. W. Humke, L. Xu, D. J. Wong, S. B. Willingham, E. J.

Schwartz, I. L. Weissman, S. S. Jeffrey, J. W. Neal, R. Rohatgi, H. A. Wakelee and S. X. Wang, *Lab Chip*, 2014, **14**, 78–88.

7 S. L. Stott, R. J. Lee, S. Nagrath, M. Yu, D. T. Miyamoto, L. Ulkus, E. J. Inserra, M. Ulman, S. Springer, Z. Nakamura, A. L. Moore, D. I. Tsukrov, M. E. Kempner, D. M. Dahl, C.-L. Wu, A. J. Iafrate, M. R. Smith, R. G. Tompkins, L. V Sequist, M. Toner, D. A. Haber and S. Maheswaran, *Sci. Transl. Med.*, 2010, **2**, 25ra23.

8 A. H. Talasaz, A. A. Powell, D. E. Huber, J. G. Berbee, K.-H. Roh, W. Yu, W. Xiao, M. M. Davis, R. F. Pease, M. N. Mindrinos, S. S. Jeffrey and R. W. Davis, *Proc. Natl. Acad. Sci. U.S.A.*, 2009, **106**, 3970–3975.

9 N. M. Karabacak, P. S. Spuhler, F. Fachin, E. J. Lim, V. Pai, E. Ozkumur, J. M. Martel, N. Kojic, K. Smith, P. I. Chen, J. Yang, H. Hwang, B. Morgan, J. Trautwein, T. A. Barber, S. L. Stott, S. Maheswaran, R. Kapur, D. A. Haber and M. Toner, *Nat. Protoc.*, 2014, **9**, 694–710.

10 S. Nagrath, L. V Sequist, S. Maheswaran, D. W. Bell, D. Irimia, L. Ulkus, M. R. Smith, E. L. Kwak, S. Digumarthy, A. Muzikansky, P. Ryan, U. J. Balis, R. G. Tompkins, D. a Haber and M. Toner, *Nature*, 2007, **450**, 1235–1239.

11 S. L. Stott, C.-H. Hsu, D. I. Tsukrov, M. Yu, D. T. Miyamoto, B. a. Waltman, S. M. Rothenberg, A. M. Shah, M. E. Smas, G. K. Korir, F. P. Floyd, A. J. Gilman, J. B. Lord, D. Winokur, S. Springer, D. Irimia, S. Nagrath, L. V. Sequist, R. J. Lee, K. J. Isselbacher, S. Maheswaran, D. a. Haber and M. Toner, *Proc. Natl. Acad. Sci. U.S.A.*, 2010, **107**, 18392–18397.

12 P. Chen, Y. Huang, K. Hoshino and X. Zhang, *Lab Chip*, 2014, **14**, 446–458.

13 M. Kagan, D. Howard, T. Bendele, J. Doyle, J. Allard, N. Tu, M. Hermann, H. Rutner, J. Mayes, J. Silvia, M. Repollet, T. Bui, T. Russell, C. Rao and L. W. M. M. Terstappen, *J. Clin. Ligand Assay*, 2002, **25**, 104–110.

14 M. Cristofanilli, G. T. Budd, M. J. Ellis, A. Stopeck, J. Matera, M. C. Miller, J. M. Reuben, G. V. Doyle, W. J. Allard, L. W. M. M. Terstappen and D. F. Hayes, *N. Engl. J. Med.*, 2004, **351**, 781–791.

15 K. Hoshino, Y.-Y. Huang, N. Lane, M. Huebschman, J. W. Uhr, E. P. Frenkel and X. Zhang, *Lab Chip*, 2011, **11**, 3449–3457.

16 P. Chen, Y.-Y. Huang, K. Hoshino and J. X. J. Zhang, *Sci. Rep.*, 2015, **5**, 8745.

17 Y. Huang, P. Chen, C. Wu, K. Hoshino, K. Sokolov, N. Lane, H. Liu, M. Huebschman, E. Frenkel and J. X. J. Zhang, *Sci. Rep.*, 2015, **5**, 16047.

18 K. Hoshino, P. Chen, Y. Y. Huang and X. Zhang, *Anal. Chem.*, 2012, **84**, 4292–4299.

19 Y. Geng, P. Dalhaimer, S. S. Cai, R. Tsai, M. Tewari, T. Minko and D. E. Discher, *Nat. Nanotechnol.*, 2007, **2**, 249–255.

20 K. Yang and Y. Q. Ma, *Nat. Nanotechnol.*, 2010, **5**, 579–583.

21 N. Hao, L. Li and F. Tang, *Biomater. Sci.*, 2016, **4**, 575–591.

22 N. J. Hao, L. F. Li and F. Q. Tang, *Int. Mater. Rev.*, 2017, **62**, 57–77.

23 J. Ma, S. M.-Y. Lee, C. Yi and C.-W. Li, *Lab Chip*, 2017, **17**, 209–226.

24 K. S. Elvira, X. Casadevall i Solvas, R. C. R. Wootton and A. J. de Mello, *Nat. Chem.*, 2013, **5**, 905–915.

25 J. Il Park, A. Saffari, S. Kumar, A. Günther and E. Kumacheva, *Annu. Rev. Mater. Res.*, 2010, **40**, 415–443.

26 N. Hao, Y. Nie and J. X. J. Zhang, *Int. Mater. Rev.*, 2018, DOI:10.1080/09506608.2018.1434452.

27 N. Hao, Y. Nie and J. X. J. Zhang, *ACS Sustain. Chem. Eng.*, 2018, **6**, 1522–1526.

28 Y. Nie, N. Hao and J. X. J. Zhang, *Sci. Rep.*, 2017, **7**, 12616.

29 N. Hao, Y. Nie, A. Tadimety, A. B. Closson and J. X. J. Zhang, *Mater. Res. Lett.*, 2017, **5**, 584–590.

30 T. Sugimoto, M. M. Khan, A. Muramatsu and H. Itoh, *Colloid. Surf. A*, 1993, **79**, 233–247.

31 T. Sugimoto, M. M. Khan and A. Muramatsu, *Colloid. Surf. A*, 1993, **70**, 167–169.

32 M. Li, X. Li, X. Qi, F. Luo and G. He, *Langmuir*, 2015, **31**, 5190–5197.

33 A. P. Sudarsan and V. M. Ugaz, *Lab Chip*, 2006, **6**, 74–82.

34 C. Vogt, M. S. Toprak, M. Muhammed, S. Laurent, J. L. Bridot and R. N. Müller, *J. Nanopart. Res.*, 2010, **12**, 1137–1147.

35 H. M. Joshi, M. De, F. Richter, J. He, P. V. Prasad and V. P. Dravid, *J. Nanopart. Res.*, 2013, **15**, 1448.

36 H. Schneck, B. Gierke, F. Uppenkamp, B. Behrens, D. Niederacher, N. H. Stoecklein, M. F. Templin, M. Pawlak, T. Fehm and H. Neubauer, *PLoS One*, 2015, **10**, e0144535.

37 B. Barlogie, M. N. Raber, J. Schumann, T. S. Johnson, B. Drewinko, D. E. Swartzendruber, W. Göhde, M. Andreeff and E. J. Freireich, *Cancer Res.*, 1983, **43**, 3982–3997.

38 N. J. Hao, L. L. Li, Q. Zhang, X. L. Huang, X. W. Meng, Y. Q. Zhang, D. Chen and F. Q. Tang, *Microporous Mesoporous Mater.*, 2012, **162**, 14–23.

39 C. H. Wu, Y. Y. Huang, P. Chen, K. Hoshino, H. Liu, E. P. Frenkel, J. X. J. Zhang and K. V. Sokolov, *ACS Nano*, 2013, **7**, 8816–8823.

40 F. Lu, S. H. Wu, Y. Hung and C. Y. Mou, *Small*, 2009, **5**, 1408–1413.

41 M. Takao and K. Takeda, *Cytom. Part A*, 2011, **79A**, 107–117.

Table of Contents
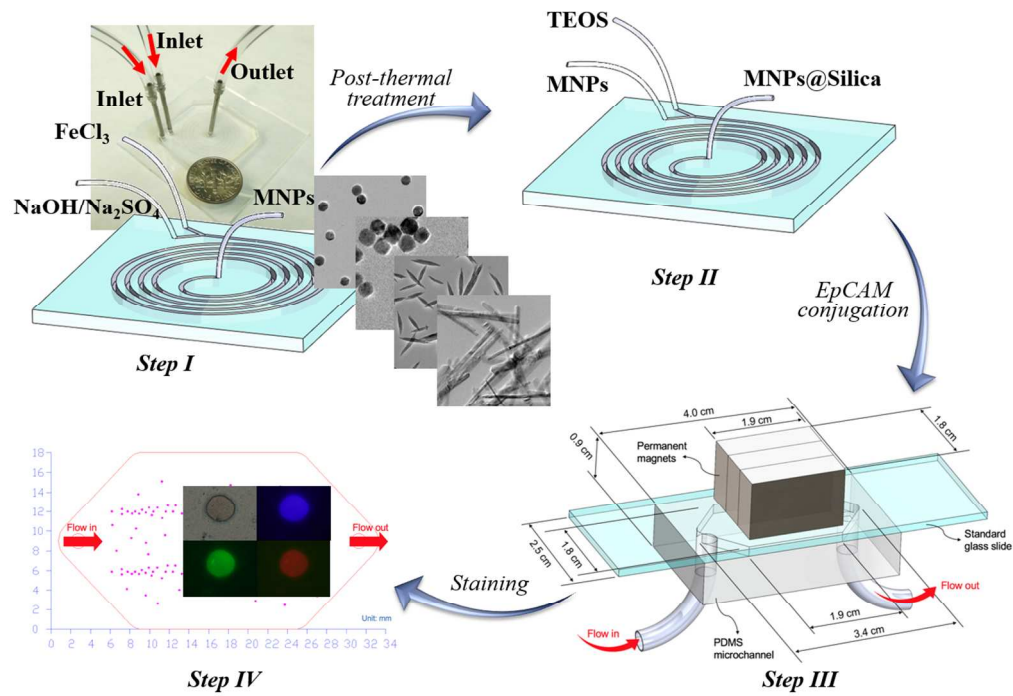
A microfluidics-enabled strategy for controllable synthesis of immunomagnetic nanomaterials was developed and the shape-dependent screening efficiency of CTCs was investigated